Received June 1995
Revised April 1996

Numerical study of 2D and 3D flowfields in a high-power pulsed chemical laser

J. Vuillon and D. Zeitoun
Département Milieux hors d'Equilibre, Institute Universitaire des Systèmes Thermiques Industriels, Université de Provence, Marseille, France

Introduction

Chemical lasers convert directly chemical energy into coherent radiation and are expected to be the most efficient and compact type of lasers in terms of cost per photon and of ratio of power to weight and volume[1]. Moreover, HF and DF pulsed chemical lasers, based on the electrical dissociation of SF_6, are very attractive because they use gases easy to handle, which are not corrosive and there is no risk of premature ignition[2]. In a high repetition pulsed mode, it is well known that to get a high quality output laser beam, it is necessary that the flow in the laser discharge zone recovers its homogeneity before the next pulse is started[3-14]. Consequently, due to the strong energy deposition during the laser pumping process, efficient removal of waste heat and effective damping of shock and acoustic waves must be achieved during the interpulse time. However, at a high repetition rate, experimental results[15] show a decrease of the output energy laser beam coupled with a pressure increase in the cavity. The short characteristic time of the laser production effect[16] by comparison with those of the flow ($t_{laser} << t_{flow}$) indicates that the output energy decrease is induced by the flow perturbations and mainly, by the residual pressure perturbations, remaining in the laser cavity after the strong electric discharge. Previous experimental studies[7-10] have shown that three types of pressure waves are propagating in the laser cavity. The first family concerns the longitudinal shock waves propagating in the flow direction due to the energy deposition needed to achieve laser pumping in the center of the laser cavity. The waves of the second family correspond to transverse acoustic waves between electrodes and are induced by the non-uniformity of the energy deposit arising from the increase of electric field and injected energy in the electrode sheaths. Finally, the third shock waves family are the axial waves travelling in the optical direction. These third family waves are inherently due to the inactive volume (no pumping) between the discharge edge and the optical window, or can also have been induced by post-discharge overdensities in the discharge volume. However these post-discharge effects which have clearly been put in evidence in excimer laser cavities[10] have not been reported so far in pulsed chemical laser devices.

International Journal of Numerical Methods for Heat & Fluid Flow
Vol. 7 No. 1, 1997, pp. 24-41.

Consequently, only the influence of the inactive volume will be taken into account in this work. Due both to the complexity of the problem involved and to the small characteristic times, about 10^{-6} s., of the shock wave processes taken into account, an accurate numerical simulation of the flowfield in the chemical laser cavity has to be carried out[17]. This approach, based on the advancement of computational techniques and computer speeds, has provided an opportunity for rapid critical design evaluations that can supplement the overall laser flow system design[4].

The present paper is divided into several sections. The second section outlines the physical problem and the relevant theoretical model. In a chemical laser, it is important to note that the presence of SF_6 in the gas mixture requires taking into account the variation of the ratio of specific heats $\gamma(T)$ as a function of temperature and consequently, the calculations are done under real gas equilibrium assumptions. The third section deals with the numerical issues related to the integration of the conservation equations. The fourth section presents the geometry, the initial conditions and the numerical resolution implemented for both 2D and 3D computations. The fifth section starts with two-dimensional results of the flow in both single shot and multidischarge operating modes. The study of vorticity production in flows with non-homogeneous density allows the extraction of information on the distortions of the contact surfaces observed in the two-dimensional results. In the sixth section, the limitations of the two-dimensional modelization are clearly put in evidence and an extension to a three-dimensional test case is developed. This extension allows taking into account the disturbances which propagate in the optical direction (family 3) and which are mainly responsible for the output laser beam decrease[4,10]. 3D numerical results are presented and comparisons between the 2D and 3D modelizations are made. The final section outlines the relevant conclusions based on the overall content of this paper.

Physical problem and theoretical model

The flowfield modelization is restricted to the laser cavity which is the head of the pulsed laser device. A schematic diagram of the chemical laser cavity is shown in Figure 1. One can clearly see on this diagram the inlet and outlet sections of the cavity which allow the correct clearing of the laser cavity discharge volume by a subsonic flow recirculation gas loop, the shape of the lower anode which permits to accelerate the flow in the discharge volume with characteristic length is ($L^*h^*L_z$), and the location of a pressure gauge. For more details on this device see Reference[2].

The unsteady subsonic flowfield in the main channel is governed by the Euler equations which can be expressed in the conservative form as:

$$\frac{\partial U}{\partial t} + \frac{\partial F^j}{\partial x_j} = 0 \qquad (1)$$

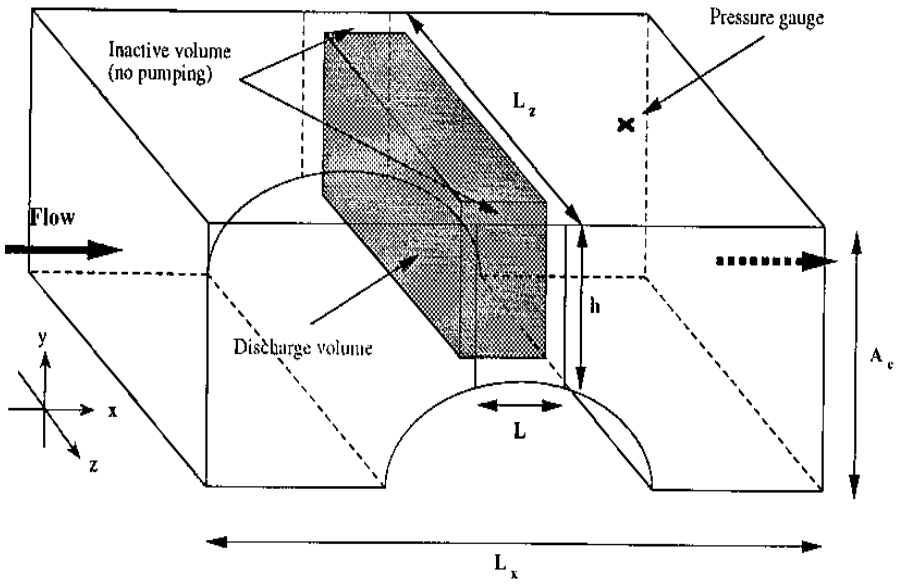

Figure 1.
Schematic diagram of the chemical laser cavity

where the summation convention has been employed and

$$U = \begin{bmatrix} \rho \\ \rho u_1 \\ \rho u_2 \\ \rho u_3 \\ \rho E \end{bmatrix}, \quad F^j = \begin{bmatrix} \rho u_j \\ \rho u_1 u_j + P\delta_{1j} \\ \rho u_2 u_j + P\delta_{2j} \\ \rho u_3 u_j + P\delta_{3j} \\ u_j(\rho E + P) \end{bmatrix} \tag{2}$$

where ρ, P and E denote the density, pressure and specific total energy, respectively, and u_j; j = 1, 2, 3 are the flow components in the respective co-ordinate directions x_j; j = 1, 2, 3 of a Cartesian co-ordinate system.

In previous works[11-13], the flow has been assumed as two-dimensional in the main channel. This assumption is based on the fact that the ratio between the optical and the interelectrode lengths L_z/h is equal to about 10. Consequently, a two-dimensional resolution is implemented by removing the integration along the third co-ordinate direction (j = 3) from the above set of equations.

Finally, in order to implement the computation, the non-regular cavity geometry (x, y, z) is usually transformed into a rectangular domain (ξ, η, ζ), where the formalism of the Euler equations is conserved[18].

To close the above set of equations, the equation of state of the gas mixture is added:

$$P=(\gamma(T)-1)\rho e \tag{3}$$

where e is the internal energy per unit mass and $\gamma(T)$ is the ratio of specific heats which is calculated under equilibrium assumptions. This is imposed by

high molar fraction of SF_6 in the gas mixture: SF_6 (45 per cent), Ne (45 per cent), H_2 (5 per cent), F(5 per cent), which requires taking into account the specific heat at constant volume variation with temperature. This variation is obtained by a curve fitting of the values given in the JANAF thermochemical tables[19]. In the range (0 – 800°K), the following equation gives the $Cv_{(SF_6)}$ polynomial evolution as a function of temperature:

$$Cv_{(SF_6)} = -1.099 + 5.605\, e^{-2T} - 5.597\, e^{-5T^2} + 1.805\, e^{-8T^3} \quad (4)$$

As concerns the numerical resolution of the above equation set (1-4), they are all treated with sequential one-dimensional solvers based on flux-corrected transport algorithms which are presented in the next section.

Numerical methods

Integration stage

For the modelization of the flow in the laser cavity, an unsteady inviscid computational approach with appropriate accuracy for nonlinear (strong shocks, contact surfaces, expansions and their mutual interactions) as well as linear regimes is required. Based on the works of Srivastava *et al.*[20], where several numerical schemes have been evaluated using model problems which are representative of laser applications, explicit difference schemes associated with flux corrected transport (FCT) algorithm have been developed for our laser computations[11-13]. The first algorithm developed was based on the SHASTA-FCT algorithm of Boris and Book[21]. Then, following the evolution of the FCT methods that we have chosen for the modelization of these pulsed laser problems, a more efficient method for the three dimensional modelization has been implemented. This last method is known as the LCPFCT method, which is a one-dimensional FCT algorithm with fourth-order accuracy and minimum residual diffusion. It has been developed by Oran and Boris[22] and was recently updated by Boris *et al.*[23].

However, for these pulsed laser flow problems, interesting comparisons between total variation diminishing (TVD) schemes and FCT schemes could be found in the recent work of Srivastava *et al.*[4].

Without going into the details of the FCT numerical schemes (available in the references cited above), one can notice that in each of the integration directions, a time split step approach is used, where the x_j; j = 1, 2, 3 directions are alternated, and each sequential integration constitutes a full convection time step. In order to carry out these sequential integrations, using the split step approach, one must ensure that the time step is small enough that the distinct components of the fluxes do not change the cell averaged values appreciably during the timestep.

Boundary conditions

As concerns the implementation of the boundary conditions, the LCPFCT and SHASTA-FCT numerical schemes are both completed by a Riemann solver for

the computation of the wall and exit boundary conditions[24]. This solver allows minimal non physical disturbances entering the inlet and outlet areas of the main channel where subsonic flow in these sections is imposed by the recirculation gas loop.

Laser cavity geometry, initial conditions and numerical resolution

Laser cavity geometry

As concerns the geometry of the laser cavity, the length of the cavity in the flow and optical directions, the gap, the width of the electrodes and the height of the boundary conditions are respectively equal to L_x = 26.5cm, L_z = 40cm, h = 3cm, L = 4cm and A_e = 5.5cm, and the location of the pressure gauge is 7.2cm from the cavity centre, Figure 1. In the two-dimensional modelization, a plane perpendicular to the optical direction including the pressure gauge, is considered and the previous real dimensions are strictly used. However, due to the large width of the cavity in the optical directions (between optics), L_z = 40cm, the three-dimensional modelization has been implemented for L_z = 10cm and L_x = 20cm, in order to get a reasonable number of grid points and CPU-time while keeping the non-regular geometry of the cavity and a ratio L_z/h greater than 2.

Initial conditions

The initial flow conditions, which are the same for the 2D and 3D modelizations, are given in Table I, and the flow parameters at the initial time are assumed isentropic. These initial conditions correspond also to the conditions implemented outside the computational domain for the resolution of the Riemann problem on the inlet and outlet areas.

Table I.
Initial flow conditions

v_0	P_0	T_0	ρ_0	$\gamma(T_0)$
10 m/s	0.15 bar	273°K	5.10^4 g/cm^3	1.179

Finally, a simulated repetition rate of 100Hz is considered, which corresponds to a 10ms interpulse time, and the average value of the discharge, deduced from experimental considerations[2], is equal to 150J/l.

Numerical resolution

As it has been outlined previously, the 2D and 3D physical domains (x, y) and (x, y, z) of the laser cavity are respectively transformed into the rectangular computational domains (ξ, η) and (ξ, η, ζ). As concerns the 2D resolution, the domain is meshed by (261 * 31) points corresponding to the physical integration space steps Δx = 0.125mm and Δy = 0.1mm in the discharge zone. In the 3D resolution, the domain is meshed with (101 * 31 * 51) points, which correspond to the physical integration space steps $\Delta x = \Delta z$ = 0.2mm and the same Δy.

The timestep integration time, imposed by the Courant Friedrich Lewis stability criterion, depends on the flow fluctuations and allows to use $\Delta t = 0.53$ μs. In order to analyse the flowfield evolution along an interpulse period, 20,000 iterations are required. For the 2D case, the CPU time for computing the flowfield along a period with the FCT algorithms is about two hours on a Cray YMP 2E supercomputer. This CPU time takes into account the previous generalized transformation and equilibrium computations and corresponds to an average value of 4.5 10^{-5} s. by iteration and grid point.

2D numerical results

Single and multidischarge configurations

To be as close as possible to the experimental energy deposition profile, various initial energy shapes of the discharge have been numerically tested[25]. From the comparisons between the one-dimensional experimental and numerical pressure evolutions given by the pressure gauge, located on the upper downstream cavity wall, Figure 1, it is possible to try to get back to the initial pressure profile induced by the discharge. The best fit of the experimental pressure evolution, in a single shot configuration, Figure 2, has been obtained with an initial injected energy profile having a maximum located near the anode wall. The average value of the discharge profile (150J/l) reproduces well the longitudinal shock wave intensity propagating from the discharge region at a local Mach number equal to 1.09. The two first wave transverse peaks, for t in the range 0.4-0.6ms, seem to be well reproduced in the computation, even if the propagation velocity is higher in the experimental data. Moreover this maximum energy deposition situated near the anode wall is consistent with the maximum energy located in the anode and cathode sheaths experimentally observed[8-10]. The local propagation shock wave Mach number is also consistent with the experimental range values obtained by Maeno[5-7].

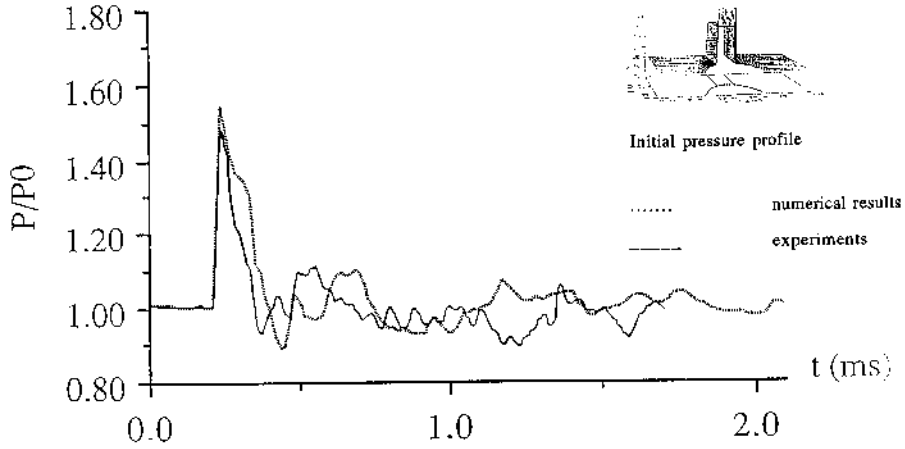

Figure 2. Comparison between numerical and experimental results given by the pressure gauge

Figure 3 shows the pressure evolution in the cavity induced by the above outlined energy deposition profile. One can notice the creation and propagation of strong longitudinal shock waves (first family) and the acoustic transverse waves (second family) induced by the non-uniform energy deposition. The longitudinal shock waves are weakly disturbed by the subsonic flow and the wave evolution is quasi-symmetric. Moreover, one can also notice a depression behind the shock waves induced by the rarefaction waves where the pressure level gets down to 0.13 bar. In order to extract informations on the interpulse period and on the initial conditions of the consecutive discharge, classical root-mean-square values $(\Delta P/P)_{rms}$ of the pressure disturbances have been employed for the characterization of the optical properties of the flowfield in the discharge zone. Practically, the pressure disturbances created by a laser pulse must be damped out to acoustic levels ($\Delta P/P < 10^{-3}$) by the time the next pulse is being injected into the device.

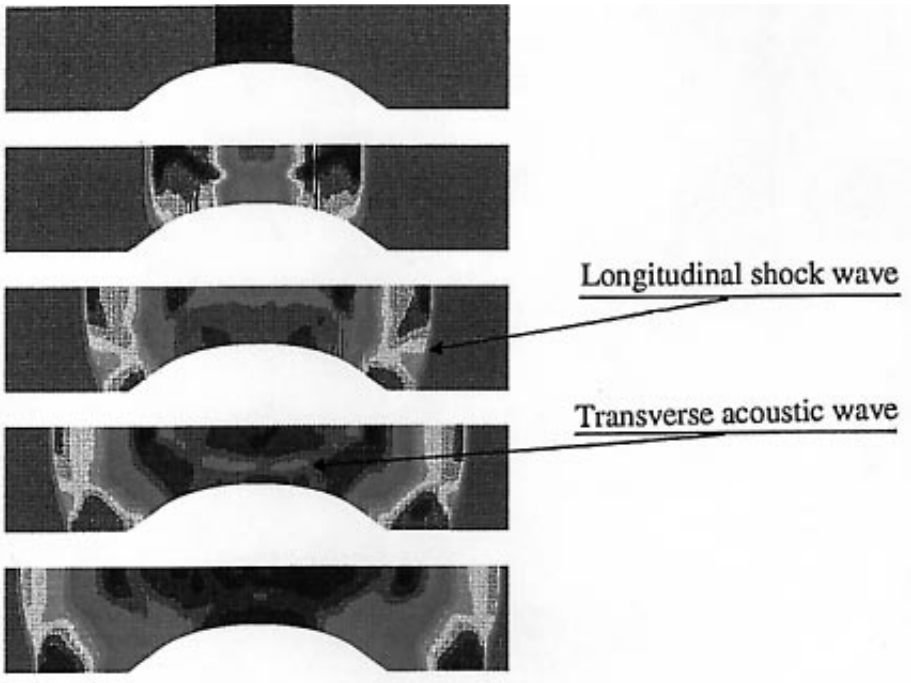

Figure 3.
Pressure evolution in the cavity at $t = 0$, $t = 0.16$, $t = 0.55$ and $t = 0.71$ms

The decay of pressure disturbances in the discharge volume for the two first discharges is shown in Figure 4. This figure is representative of the pressure evolution in the cavity, which can be divided in two separated processes. The first one, before 1.5ms, is characteristic of a free diffusion wave process in the cavity, as shown in Figure 3. Due to the elliptic shape of the lower electrodes, transverse acoustic waves, generated by the non-uniform energy deposition, are rapidly attenuated and evacuated out of the discharge zone through the successive reflections. Then, after 1.5ms, a reverberation process of the waves in

the cavity is observed[8-10]. The pressure perturbation level decreases less rapidly during this second process. However, an acoustic level of the pressure disturbances is finally reached for t = 7ms. This weak level is mainly responsible for the similar evolution of the decay of pressure disturbances for the two first discharges shown in Figure 4. At t = 10ms, the homogeneity of the flowfield is high enough to ensure the quality of the output energy laser beam. From this evolution of the pressure disturbances in the discharge zone, one can see here one of the limitations of the two-dimensional modelization that will be developed in the next section.

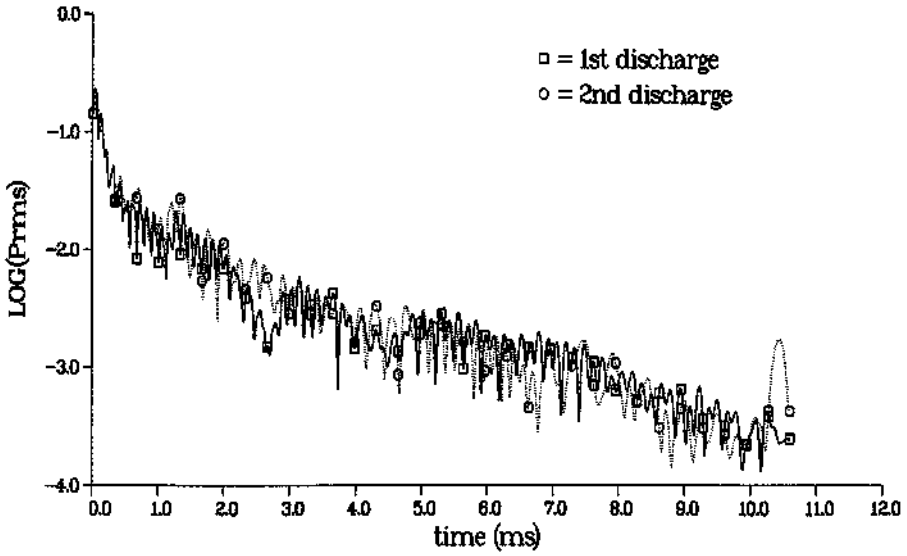

Figure 4. Decay of pressure disturbances in the discharge zone, average discharge energy injected 150J/l

As concerns the flowfield evolution in the cavity, for this multidischarge process, the complex flow is represented through a plot of temperature isovalues at different time intervals, Figure 5. One can retrieve here the shape of the initial energy deposition outlined above, with a maximum located near the lower electrode wall. Consequently, the temperature in the discharge zone grows up to 503°K in the middle and up to 630°K in the vicinity of the wall. The increase of the internal energy of the gas during the energy deposition, due to the presence of SF_6 in the mixture, makes first the hot column gas created to extend itself by a factor of 1.7 which is clearly shown in the second picture of Figure 5. This behaviour, which is proper to the HF/DF chemical laser, has never been observed in the previous study concerning an excimer laser[5-11]. For the laser system device, this expansion leads to an increase of the velocity in the cavity in order to ensure a correct clearing ratio of the discharge zone. After this expansion, the hot column gas is entirely evacuated by the flow out of the discharge zone within 8ms. As concerns the flow evolution, the distortions of the hot column gas, in the vicinity of the lower electrode, have first been explained by the shape of the

cavity which accelerates the flow in the discharge zone and decelerates it in the downstream part of the cavity. However, a similar evolution of the contact surfaces has also been observed in the vicinity of the straight upper cavity wall[25] and such an evolution of the flow can no longer be due to the geometric shape of the cavity only. Consequently, it has been pointed out that the distortions of the hot column gas created come from the non-uniform energy deposition profile which induces interactions between strong density and pressure gradients. It is well known that the interaction of pressure waves with density fluctuations in a fluid is a major source of vorticity and turbulent motion[13, 26]. In addition to that, these rotational flows evolve on much longer timescales than that of shock propagation through a local non-uniformity and can have an important long-term effect on the structure and properties of the flow.

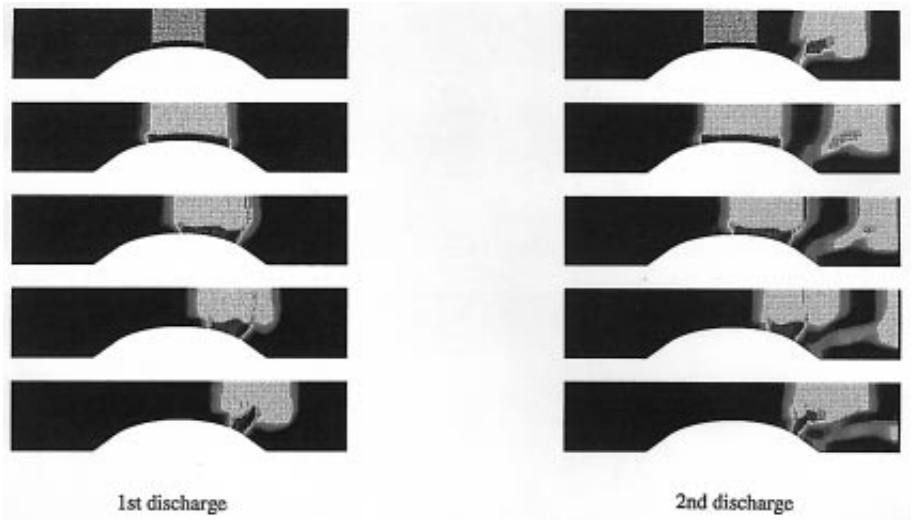

Figure 5.
Temperature evolution in the laser cavity at t = 0, t = 1.06, t = 4.24, t = 7.42, t = 9.54 ms (first discharge), t = 10, t = 11.06, t = 14.24, t = 17.42, t = 19.54 ms

In order to better understand the evolution of the temperature isovalues shown in Figure 5, the above-mentioned pressure and density interaction effects have been studied using the following basic equation which governs the evolution of vorticity in an inviscid fluid. This equation is deduced from a non-linear theory of shock-generated vorticity recently developed by Picone *et al.*[26]:

$$\frac{\partial \vec{\omega}}{\partial t} + \vec{u}.\vec{\nabla}\vec{\omega} = \frac{1}{2}\vec{\omega}(\vec{\nabla}\vec{u}+\vec{\nabla}\vec{u}^{t}) - \vec{\omega}\vec{\nabla}.\vec{u} + \frac{1}{\rho^2}\vec{\nabla}\rho\wedge\vec{\nabla}P \qquad (4)$$

In the above equation, $\vec{u}$ and $\vec{w}$ are the flow and vorticity vectors. Considering the right hand of equation (4), one can notice that a misalignment of the local pressure and density gradients leads to a non-zero source term $S = 1/\rho^2\ \vec{\nabla}\rho\wedge\vec{\nabla}P$. The other source terms are non-zero only in case of vorticity already present in the flowfield. In our modelization, these other source terms do not play an important role.

In order to clearly put in evidence the contact surface distortions between hot and cold gas, a numerical simulation has been carried out in a rectangular cavity, with a non-uniform discharge in the longitudinal direction and with a zero-velocity initial flow. In Figure 6, one can see the initial discharge profile and its evolution in time through the plot of temperature isovalues. The deformation of the contact surface and the creation of contra-rotating vortices are clearly visible. This flowfield evolution allows explanation of the evolution of the two hot column gas shown in Figure 5, where the non-uniform energy deposition along the transverse direction leads to similar effects. The misalignment of pressure and density gradients, induced by the electric discharge, leads to vorticity production with a characteristic time less than 1ms and to flowfield disturbances through vortex creation with a characteristic time decay equal to the interpulse period (10ms).

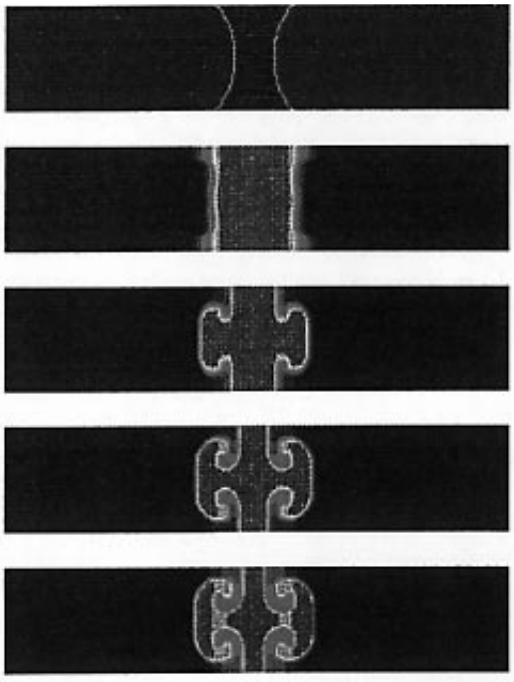

Figure 6. Vortices production through temperature evolution in rectangular cavity with zero-initial velocity flow at $t = 0$, $t = 2.12$, $t = 4.24$, $t = 7.42$, $t = 10.63$ ms

The flowfield evolution during the second discharge is also presented in Figure 5. One can see the second hot gas column created by the energy deposition and its evolution in time at the same timestep as in the first discharge. The same evolution in the lower downstream part of the computational domain is noticed even if the heated gas produced by the second discharge is more distorted than the first one. These distortions come first from the vorticity already present in the cavity due to the first energy deposition, and second from the direct interactions of the pressure waves produced by this second discharge with the density fluctuations inherently evacuated to the downstream part of the cavity.

However, the discrepancies shown here between the first and the second hot gas column evolution tend to attenuate when this multidischarge process is carried over three or four pulses, and reproductibility of the flow between two consecutives pulses is finally obtained[25]. In addition, one can notice the correct evacuation of the subsonic heated flow outside the computational domain as the boundary conditions are described by a Riemann solver.

Limitations of the 2D approach and extension to a 3D modelization

Limitations of the 2D approach

On one hand, from the analysis of experimental results obtained in multidischarge operating mode with both chemical[2,15] and excimer[8-10] lasers, one can mainly notice the asymptotic rise of the pressure in the cavity, which finally reaches a maximum level. This maximum level seems to be characteristic of the laser device employed. Note that in the HF/DF chemical laser, the laser cavity, whose average volume is approximately 5 l, is entirely contained in a stainless steel cylindrical vessel, whose characteristic volume is 400 l (see reference[2]). Due to the fast rise of the pressure in the cavity, with a duration of 0.5s at a 60Hz repetition rate frequency, the maximum pressure level reached comes directly from the laser cavity volume which is the head of the laser system device. Moreover, when the repetitive discharge process is stopped, the pressure evolution is characteristic of an exponential relaxation process $e^{-t/\tau}$. In the same time, the decrease of the output energy laser beam is clearly coupled to the accumulation of strong pressure disturbances in the cavity.

On the other hand, the numerical reproductibility of the flowfield using a two-dimensional modelization has been shown in the previous section for both pressure (Figure 4) and temperature evolutions (Figure 5). As a consequence, one should think that the pressure increase in the cavity observed experimentally, is mainly induced by pressure disturbances propagating in the optical direction. In addition, these disturbances, such as shock waves generated in the inactive volume of the discharge zone, (Figure 1), have a long characteristic relaxation time. Consequently, in order to quantify the influence of the optical direction, an extension of the numerical approach to a tridimensional modelization has been carried out.

Extension to a 3D modelization

Algorithm considerations

Prior to the extension to the 3D modelization, several accuracy tests have been carried out, for given related laser problems, in an effort to identify an appropriate numerical procedure (algorithm, space and time steps employed) with desired accuracy for this extension[25]. Consequently, following the evolution of the FCT methods, the high order, monotone, conservative, positivity preserving LCPFCT algorithm[22,23] has been adapted for the chemical laser flowfield 3D modelization. Besides, in order to achieve the extension to the 3D case with a reasonable number of grid points, both the longitudinal and optical directions, L_x and L_z have been reduced to respectively 20cm and 10cm.

Influence of the space and time steps:
The influence of the parameters of the 3D modelization has been tested here in an effort to keep a non prohibitive CPU-time. Through the longitudinal and optical dimensions L_x and L_z chosen above, several two-dimensional modelizations have been carried out to study the eventual non-physical spreading of the discontinuities (shock waves, contact surfaces…) as function of the space steps. Figure 7 shows the $(\Delta\rho/\rho)_{rms}$ evolution in time, for a non-uniform energy deposition with average value 150J/l, and for space steps in the range 1mm-4mm. As concerns the density evolution, for Δx smaller than to 2mm, one can clearly see the expansion of the hot gas column created and its evacuation on the downstream part of the cavity. However, when the space step is greater equivalent than 3mm, the contact surface between the heated gas and the cold initial gas is totally smoothed over the grid points while the loss of accuracy increases in the same proportion as the space steps. Thus, for the 3D modelization and for the laser related problem, the space between the grid points cannot reasonably exceed 2mm.

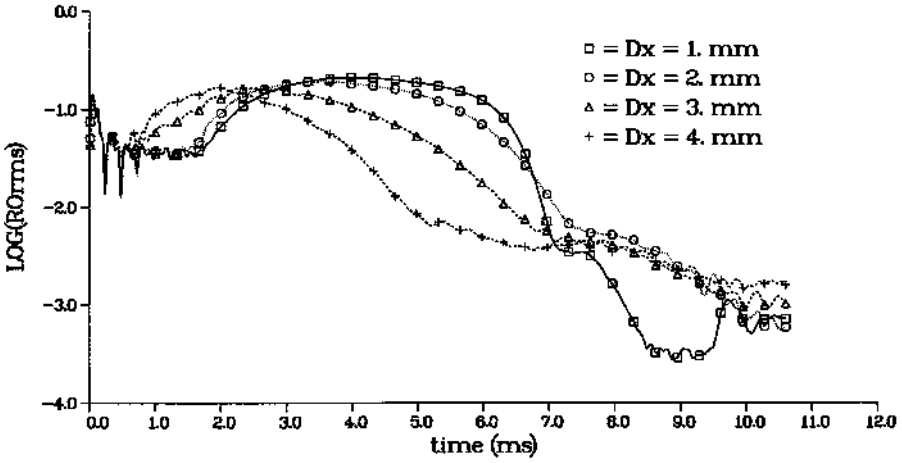

Figure 7. Influence of the space step in the longitudinal direction on the decay of density disturbances in the discharge zone, 2D chemical laser cavity, average discharge energy injected 150 J/l

Another way to reduce the CPU-time, while respecting the CFL criterion, consists in increasing the timestep of the modelization. At the initial time, where the strong electric energy deposition is introduced, a limit of the maximum value of the integration time step Δt is imposed and corresponds to $\Delta t = 3.88\mu s$. Several accuracy tests of the space steps have been done[25] for CFL values in the range $0.13 < CFL < 0.78$. For these values, the increase of the explicit integration time step does not influence significatively the propagation of the discontinuities in the chemical laser cavity. Consequently, the 3D numerical simulation has been finally implemented with $\Delta t = 2.12ms$ (CFL = 0.54) and 5,000 iterations are required to compute the flowfield over a 10ms interpulse time.

Comparisons of 2D-3D numerical results

The comparisons developed in the following allow the influence of strong perturbations travelling in the optical direction to be extracted. In the excimer laser[10], experimental results clearly show a non-uniform energy deposition along the electrodes due to electric post-discharge overdensities which strongly affect the output energy laser beam. However, in the HF/DF chemical laser, such inhomogeneities have never been reported so far and only the inactive volume between the electrode edge and the optical window, Figure 1, can produce strong disturbances travelling between optics[2,15]. As a consequence, a 2cm side effect of the electrodes has been implemented at the initial time of the modelization.

A simultaneous representation of (*xoy*) and (*xoz*) two-dimensional plane-cuts has been used to show the propagation of strong pressure waves in the cavity volume, Figure 8. One can clearly see the initial energy deposition in the

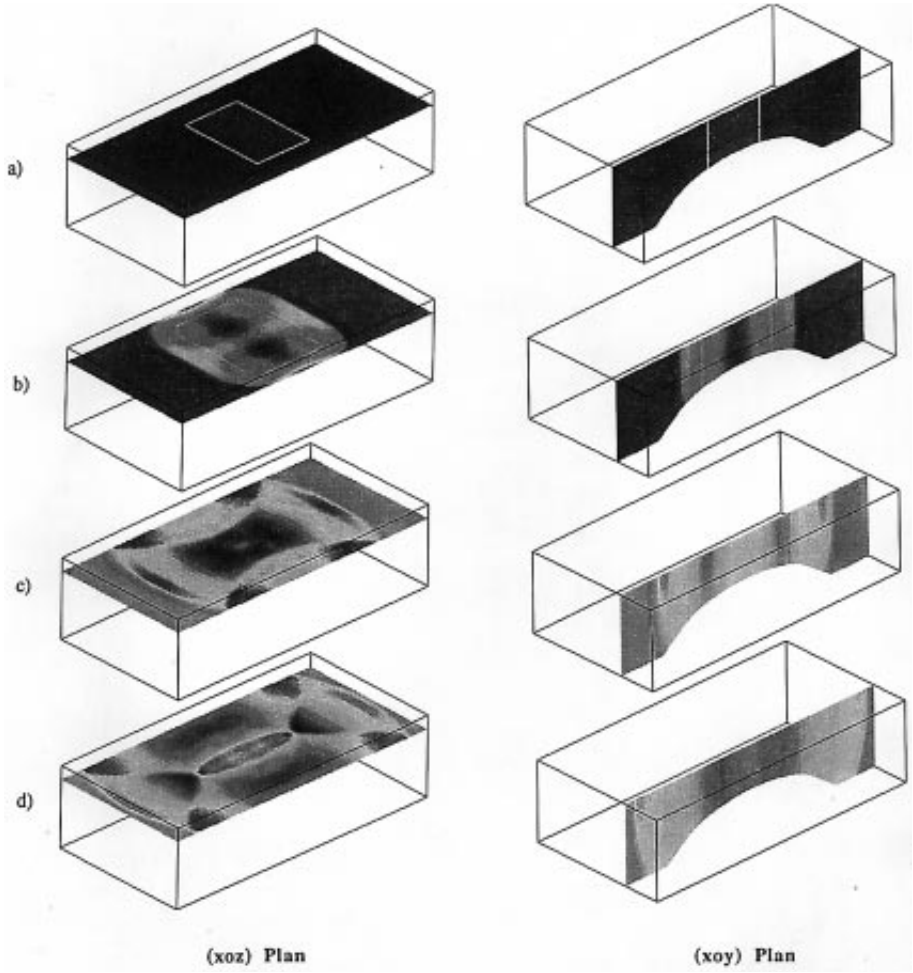

Figure 8.
Shock waves travelling in the laser cavity volume on (*xoz*) and (*xoy*) planes at $t = 0$, $t = 0.21$ ms, $t = 0.42$ ms, $t = 0.63$ ms

discharge volume, with a gap corresponding to the zone where no optical pumping has been achieved, between the edges of the electrodes and the cavity walls, (Figure 8a). The average value of the injected energy is 213 J/l and the profile is assumed to be homogeneous in the transverse direction (between the electrodes), in order to separate the influence of non-uniform energy deposition between optics and between the electrodes. This initial energy deposition profile leads to the creation and propagation of strong pressure waves in both optical and longitudinal directions. First, in the optical direction, a perfect reflection, on the cavity wall, of the cylindrical shock waves created is clearly shown in Figure 8 (b), (c) and (d). Second, in the flow direction, where nothing disturbs the propagation of the discontinuities, one can see the evacuation of the longitudinal waves out of the cavity volume as in the 2D modelization.

A comparison of the decay of pressure disturbances in the discharge volume, between the 2D and 3D computations is shown in Figure 9. The strong pressure waves travelling in the optical direction, generated by the side effect of the electrodes, lead to an increase of the perturbation level. Before 2ms, this perturbation level corresponds to the free diffusion process of the waves, such as the evacuation out of the discharge volume of the first family shock waves (Figure 8). Then, the periodic nature of the decay of pressure disturbances in the discharge volume is characteristic of the numerous reflections of the third family of acoustic waves between the optics. After 2ms, this 3D effect tends to amplify the reverberation process of the waves in the cavity, which finally gives a one order of magnitude difference between the two modelizations. The residual perturbation level in the 3D test case is equal to 10^{-2}, which is above the acoustic perturbation level required for this high repetitive rate device, instead of 10^{-3} in the two-dimensional modelization. Besides, a comparison between the 2D and 3D modelizations is made on the one-dimensional pressure evolution given by the pressure gauge situated on the upper cavity wall (Figure 10). As it has been shown in Figure 8, the initial energy deposition profile (213 J/l) creates a cylindrical shock wave propagating from the discharge volume. The two main peaks of pressure shown in Figure 10 correspond to the cylindrical shock wave (first family, t = 0.22 ms) and the head of the shock wave travelling between optics (third family, t = 0.37 ms).

However, in the 3D computation, the magnitude of the longitudinal shock wave (P/P_0 = 1.47) is less than the 2D computation (P/P_0 = 1.76). This is inherently due to the new propagation direction of the shock waves offered by the side effect of the electrodes. Then, after 0.5 ms, the pressure gauge corresponds to the numerous reflections of the cylindrical shock waves on the optics, Figure 8, and which have also been experimentally put in evidence in both chemical and excimer lasers[2,10]. Consequently, the magnitude of the pressure peaks decreases slowly in time and consists in the reverberation process of the waves. Moreover, due to the factor 4 reduction of the optical direction (L_z = 10 cm), the transit time of the waves travelling between optics is also reduced by the same factor. As a consequence, the perturbation level obtained at t = 2.5 ms in this 3D test case is consistent with the perturbation

level eventually obtained at t = 10 ms in the real case (L_z = 40 cm). From Figures 9 and 10, it is evident that the homogeneity of the flowfield at t = 2.5 ms is far from the acoustic level and this flow structure can partially explain the decrease of the output laser energy observed experimentally. Finally, a 3D multidischarge process taking into account the above-mentioned side effect of the electrodes has been implemented with a frequency eight times higher: f = 800 Hz. At the same time, the flow velocity on the throat has been similarly increased in order to ensure the same clearing ratio of the discharge volume: v = 80 m/s.

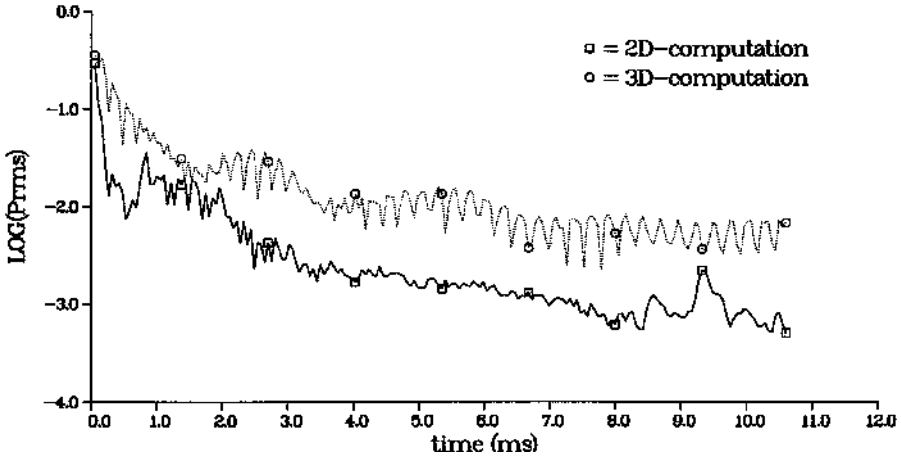

Figure 9.
Influence of the 3D side effect of the electrodes on the decay of pressure disturbance in the discharge volume, in comparison with a 2D test case, average discharge energy injected 213 J/l

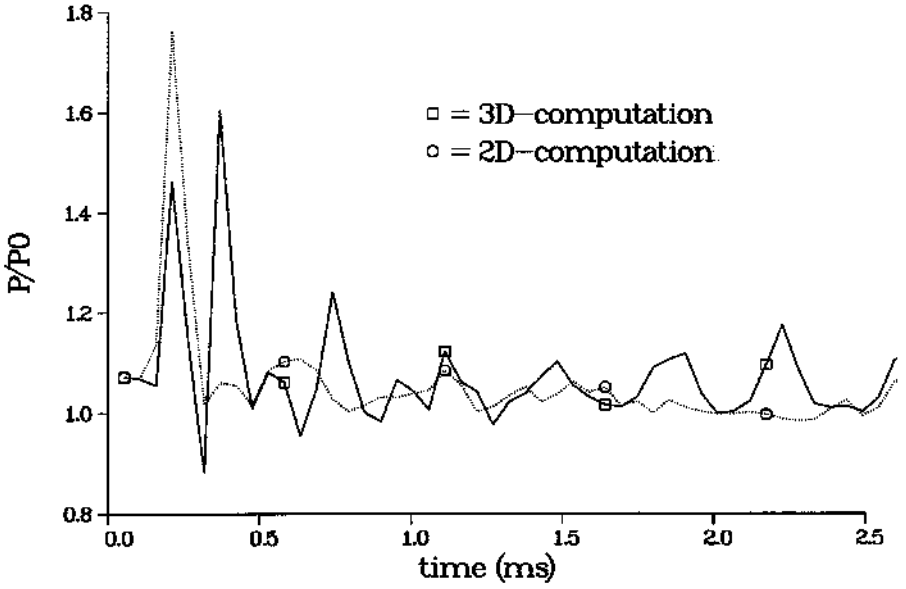

Figure 10.
Comparison of the 2D and 3D pressure evolution given by the pressure gauge, average discharge energy injected 213 J/l

The pressure evolution given by the pressure gauge is plotted in Figure.11. One can clearly see in this Figure the shot to shot amplification of the pressure in the cavity due to the strong disturbances travelling in the optical direction. Before 1.4 ms, the evolution of the pressure, corresponding to the cylindrical shock wave which propagates from the discharge volume, is the same as in Figure 8 and Figure 10. However, for this 3D multidischarge process with a frequency of 800Hz, the second peak of pressure (third family) is mainly amplified by the successive energy deposition, an 18 per cent amplification is noticed between the first (t = 0.37 ms) and the third discharge (t = 3.0 ms) and such an evolution clearly shows the influence of the side effect of the electrodes when high repetitive rates are maintained in the high-power pulsed chemical laser.

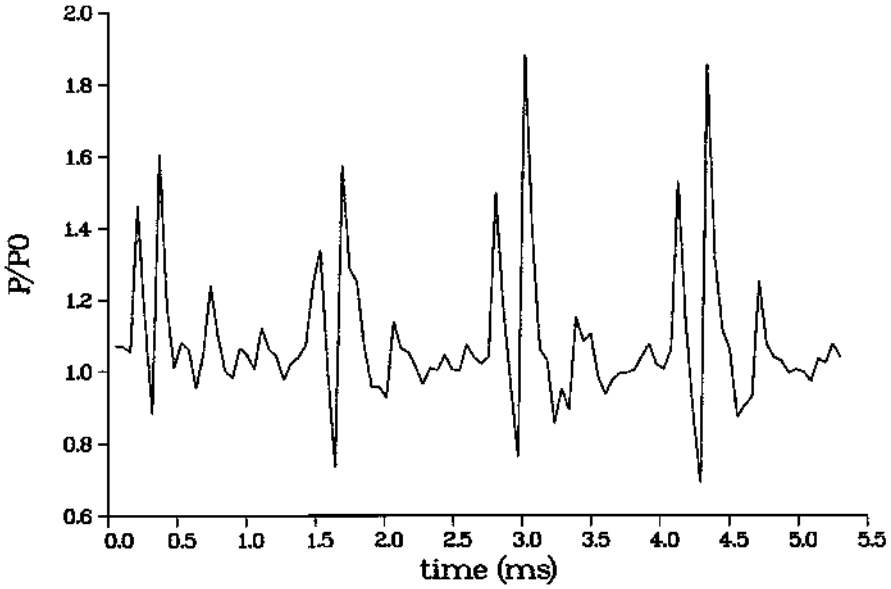

Figure 11. Pressure evolution given by the pressure gauge, 3D multidischarge process, f = 800Hz, average discharge energy injected 213 J/l

Conclusion

In this contribution, a numerical description of 2D and 3D unsteady flows in a chemical laser, taking into account the non-regular cavity shape, has been presented. The flow in the laser cavity, governed by the Euler equations, is solved under equilibrium assumptions with FCT methods. These methods are associated with a Riemann solver for the correct implementation of the boundary conditions.

Numerical computations were carried out for a two-dimensional modelization of the flow in a section perpendicular to the optical direction. An initial energy deposition profile with a maximum located in the vicinity of the elliptic lower wall has been assumed by the best fitting of single shot experimental results. However, when performing multidischarge configuration runs, the pressure

perturbation level always reaches the acoustic level by the time the next pulse is being injected into the device. The reproductibility of the numerical experiments between two pulses, due to the weak residual perturbation level, clearly puts in evidence the limitations of the two-dimensional modelization. As a consequence, this model can no longer explain the experimentally observed pressure increase in the cavity.

Studying the evolution of vorticity, one can see that a non-uniform spatial discharge in the longitudinal direction x and a non-uniform energy deposition in the transverse direction y produce the same long-time effects on flowfield behaviour. The distortions of the contact surfaces can be explained through the non linear theory of vorticity production.

A 3D modelization is finally presented in order to take into account a new propagation direction. Prior to the extension to a 3D modelization with the LCPFCT algorithm, the influence of the space and time steps is discussed in order to implement a non-prohibitive 3D modelization. Comparisons of 2D-3D numerical results are done in order to study the influence of pressure waves travelling in the optical direction, generated by the side effect of the electrodes. The increase by one order of magnitude of the decay of pressure disturbances in the 3D case compared to the 2D case, and the shot to shot amplification of the pressure peak observed in a high repetition rate mode, clearly validates the non-trivial influence of the optical direction on the output energy laser beam decrease.

Acknowledgements

Funding support from Direction des Recherches Etudes et Techniques, Groupe IV 01 is gratefully acknowledged. The authors would also like to thank the Centre de Calcul de St Jérôme for allowing access to the IBM 3090 VF.

References

1. Rosenwacks, S., "The search for short-wavelength chemical lasers – an overview", *9th International Symposium on Gas Flow and Chemical Lasers 1992*, SPIE, Vol. 1810, 1992, pp. 232-39.
2. Brunet, H., Mabru, M and Vannier, C., "Repetitively-pulsed HF chemical laser with high average power", *9th International Symposium on Gas Flow and Chemical Lasers,* SPIE, Vol. 1810, 1992, pp. 273-76.
3. Ausherman, D. R., Alber, I. E. and Baum, E., "Acoustic suppression in a pulsed chemical laser", *AIAA Journal,* Vol. 17 No. 5, 1978, pp. 490-97.
4. Srivastava, B., Faria-e-Maia, F., Her, J. and Moran, J., "High resolution computation of 2D/3D unsteady flow field in pulsed lasers", *AIAA Paper,* 1990, pp. 90-1508.
5. Kosugi, S., Ohishi, T., Maeno, K. and Honma, H., "Experimental study on shock waves in the cavity of an excimer laser", *Shock Waves Proceedings*, Sendai, Japan, 1991, pp. 1295-300.
6. Kosugi, S., Maeno, K. and Honma, H., "Effects of xenon gas on generation and propagation of shock waves in the cavity of excimer laser", *9th International Symposium on Gas Flow and Chemical Lasers*, SPIE 1810, 1992, pp. 217-20.
7. Kosugi, S., Ohishi, T., Maeno, K. and Honma, H., "Shock waves in the cavity of excimer laser of Xe-He inclusion", *Shock Waves Proceedings*, Marseille, France, 1993.

8. Delaporte, P., Fontaine, B., Forestier, B., Sentis, M., Truong, J-P., Uteza, O., Zeitoun, D. and Tarabelli, D., "Acoustics and shock waves effects in high average power excimer lasers", *Shock Waves Proceedings*, Sendai, Japan, 1991, pp. 1301-06.
9. Truong, J-P., Sentis, M., Delaporte, P., Forestier, B., Fontaine, B., Uteza, O. and Tassy, Y., "Efficient acoustic wave damping in a high pulse repetition rate XeCl laser", *9th International Symposium on Gas Flow and Chemical Lasers*, SPIE, Vol. 1810, 1992, pp. 430-4.
10. Truong, J-P., Uteza, O., Sentis, M., Delaporte, P., Forestier, B. and Fontaine, B., "Aerothermodynamic phenomena in a high pulse repetition rate XeC laser", *Shock Waves Proceedings*, Marseille, France, 1993.
11. Tarabelli, D., Zeitoun, D. and Forestier, B., "Damping on shock and acoustic waves in an unsteady two-dimensional flow", *Shock Waves Proceedings*, Sendai, Japan, 1991, pp. 1301-6.
12. Zeitoun, D. and Vuillon, J., "Flowfield modelization and simulation on pulsed chemical laser", *9th International Symposium on Gas Flow and Chemical Lasers,* SPIE, Vol. 1810, 1992, pp. 170-3.
13. Vuillon, J. and Zeitoun, D., "Wave propagation and flowfield instabilities in a high-power pulsed chemical laser", in Taylor, C. (Ed.), *8th International Conference in Numerical Methods in Laminar and Turbulent Flow,* VIII Part 2, Pineridge Press, Swansea, 1993, pp. 1587-98.
14. Vuillon, J. and Zeitoun, D., "3D modelization of shock waves in a high-power pulsed chemical laser", presented at the *10th International Symposium on Gas Flow and Chemical Lasers*, Friedrichshafen, Germany, September 1994.
15. Brunet, H. and Mabru, M., "High energy – high average power pulsed HF/DF chemical laser", presented at the *10th International Symposium on Gas Flow and Chemical Lasers,* Friedrichshafen, Germany, September 1994.
16. Anderson, D.J., "Gasdynamics lasers: an introduction", in *Quantum Electronics Principles and Applications*, Academic Press, New York, NY, 1976.
17. Oran, E.S. and Boris, J.P., *Numerical Simulation of Reactive Flow*, Elsevier, New York, NY, 1987.
18. Anderson, D.A. and Tannehill, J. C., *Computational Fluid Mechanics and Heat Transfer,* Computational Methods in Mechanics and Thermal Sciences Series, McGraw-Hill, New York, NY, 1984.
19. Stull, D.R. and Prophet, H., *JANAF Thermochemical Tables*, 2nd ed., NSRDS-NBS37, June, 1971.
20. Srivastava, B. N., Waldman, G., Cruickshank, J. and Moran, J., "Several numerical schemes for the computation of unsteady flow in pulsed lasers", *AIAA Journal,* Vol. 25 No. 6, 1987, pp. 845-54.
21. Boris, J.P. and Book, D.L., "Flux-corrected transport I, SHASTA-A fluid transport algorithm that works", *Journal of Computational Physics,* Vol. 11 No. 38, 1973.
22. Oran, E.S. and Boris, J.P., *Numerical Simulation of Reactive Flow*, Elsevier, New York, NY, 1987.
23. Boris, J.P., Landsberg, A.M., Oran, E.S. and Gardner, J.H., *LCPFCT – a Flux Corrected Transport Algorithm for Solving Generalized Continuity Equations*, Laboratory for Computational Physics and Fluid Dynamics, Naval Research Laboratory Report, April 1993.
24. Saurel, R., Larini, M. and Loraud, J.C., "Exact and approximate Riemann solvers for real gases", *Journal of Computational Physics,* Vol. 112 No. 1, 1994, pp. 126-37.
25. Vuillon, J., "Modélisation et simulation numérique des écoulements confinés eulériens instationnaires", PhD thesis, Dept Milieux hors d'Equilibre, Université de Provence, Marseille, France, Juillet, 1994.
26. Picone, J. M., Oran, E. S., Boris, J. P. and Yung, T. R., "Theory of vorticity generation by shock wave and flame interactions", *Dynamics of Shock Waves Explosions and Detonations,* AIAA, NY, 1985, p. 429.